ANNALS OF GEOPHYSICS, 69, 2026; doi:10.4401/ag-9545
OPEN ACCESS

Source Characteristics of the Mw 4.3 and Mw 4.4 central San José Earthquakes Derived from Empirical Green's Functions, Costa Rica

Aaron Moya[*,1]

(1) Universidad de Costa Rica, Laboratorio de Ingeniería Sísmica, Costa Rica

Article history: received February 12, 2026; accepted May 6, 2026

Abstract

We investigated the source characteristics of the August 22, 2025 (Mw 4.3) and January 19, 2026 (Mw 4.4) San José earthquakes in Costa Rica. Although moderate in magnitude, both events occurred at a shallow depth (~4.0 km) beneath the central urban area of the capital city. They produced strong ground shaking with peak ground accelerations reaching approximately 230 gal. Using small aftershocks as Empirical Green's functions (EGFs), we estimated the size of the strong-motion generation areas (SMGAs), rise time, rupture velocity, and associated stress drop for each event. Despite their similar magnitudes, the two earthquakes exhibit notable differences in SMGA size and stress drop, which appear to control the spatial distribution of observed acceleration.

Keywords: Strong Motion Generation Area; Fault; Accelerograph; Earthquake; Stress Drop

1. Introduction

Urban areas located in tectonically active regions face a particular risk from earthquakes due to high population density and concentration of critical infrastructure. Understanding seismic hazard in such environments is therefore essential for effective risk mitigation and urban planning, particularly where active faults are poorly expressed at the surface or remain insufficiently studied. The capital city of Costa Rica, San José, is of particular interest in this sense because the urban development has often outpaced detailed seismotectonic investigations (Peraldo and Montero, 1999; Climent et al., 2008).

Although the country lies within a highly active tectonic setting controlled by the interaction of the Cocos, Caribbean, and Panama microplates, no major active faults have been clearly identified directly beneath San José, or they remain poorly constrained (Fernández and Montero, 2002). Nevertheless, historical and instrumental seismicity demonstrates that the Greater Metropolitan Area (GAM) is exposed to significant earthquake hazard (Hidalgo-Leiva et al., 2022; Benito et al., 2025).

Historical seismicity reveals the potential consequences of earthquakes in the GAM. The most damaging event was the Ms 6.4 Cartago earthquake of May 4, 1910 (IMM VIII). It devastated the city of Cartago, located approximately 20 km east of San José. Intensity studies and historical accounts indicate near-total destruction of the city and approximately 700 fatalities, making it the most disastrous earthquake in Costa Rican history (Montero

and Miyamura, 1981; Peraldo and Montero, 1999; Alonso-Henar et al., 2013). This event serves as a clear reminder of the catastrophic impact that a shallow crustal earthquake can have on urban centers.

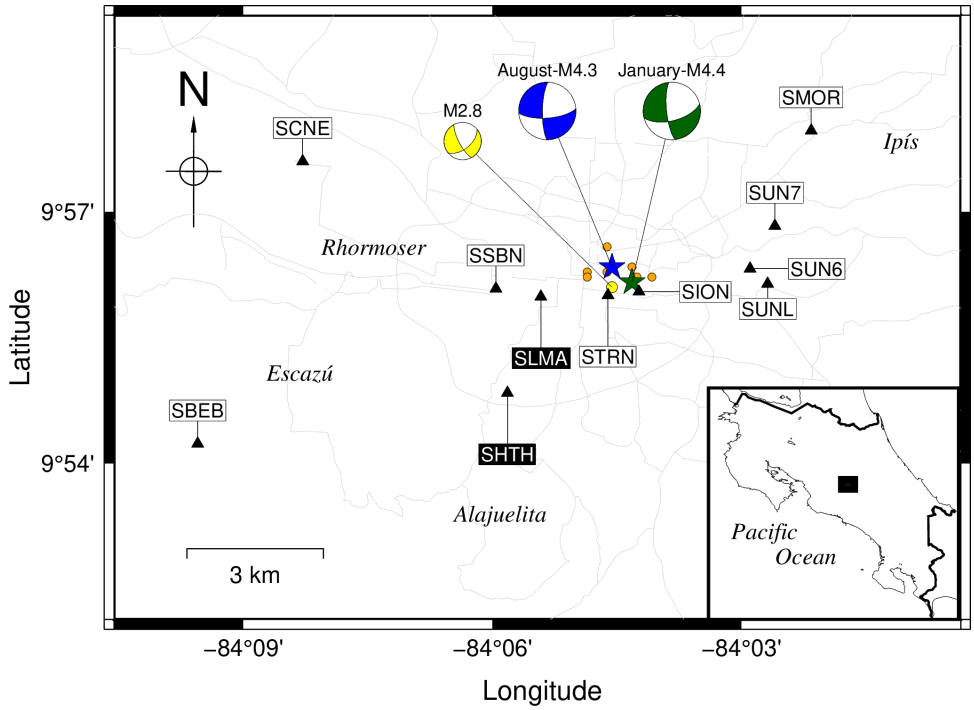

Figure 1. Seismicity recorded in central San José, Costa Rica from August, 2025 until January, 2026. The map shows the epicentral locations of the two significant events: the August 22, 2025 (Mw 4.3) (blue star) and the January 19, 2026 (Mw 4.4) (green star). The yellow circle shows the August 22, 2025 Mw 2.8 event used as empirical Green's function (EGF). Orange circles correspond to recorded aftershocks. Gray lines correspond to major roads. Focal mechanism solutions indicate a predominance of left-lateral strike-slip faulting. Black triangles show the location of the strong motion stations used in this study. SHTH and SLMA were not part of the EGF analysis. The inset map highlights the study area within Costa Rica.

The most recent Mw 6.1-6.2 Cinchona earthquake of January 8, 2009, located approximately 30-40 km north-northwest of San José (Barquero, 2009) shook the city violently. A station located some 13-14 km away from the epicenter recorded a value of 658 gals and 26.5 cm/s. This shallow, oblique-slip event generated strong ground shaking and extensive landslides, particularly on the steep volcanic slopes near the epicentral area (Quesada-Román and Barrantes-Castillo, 2016). Estimates from the Comisión Nacional de Emergencias (CNE) and national media indicate around 25-27 confirmed deaths, at least five missing, and approximately 100 injured, with hundreds of people displaced or sheltering in emergency accommodations after structural failures and slope collapses blocked access routes and damaged homes. More than 2,300 structures were damaged, with nearly 800 destroyed.

In this context, the earthquakes that took place on August 22, 2025 and January 19, 2026, directly beneath the city of San José, provide a particularly informative case study (Fig. 1). The Laboratorio de Ingeniería Sísmica at the Universidad de Costa Rica (LISUCR) estimated the magnitudes as Mw 4.3 and Mw 4.4 for the first and second events, respectively. The Red Sismológica Nacional (RSN, Universidad de Costa Rica) reported slightly higher magnitudes of Mw 4.4 and Mw 4.5, while the Observatorio Vulcanológico y Sismológico de Costa Rica (OVSICORI-UNA, Universidad Nacional) estimated their magnitude as Ml 4.1 and Ml 4.4 respectively. Despite the small differences, all three institutions consistently indicated that the first event was smaller than the second one.

Those events and some of their aftershocks were recorded by a dense strong-motion network deployed by the LISUCR across the city (Fig. 1). This allowed for high-resolution observations of near-source ground motions close to the source area. Despite their moderate magnitude, each earthquake produced notable peak ground accelerations (PGA) and velocities (PGV) throughout the GAM as shown in Fig. 2. The largest PGA and PGV values are systematically observed at stations located east of the epicenter.

In this analysis, we apply an empirical Green's function (EGF) approach using a nearby small aftershock, Mw 2.8, with similar focal mechanism and hypocentral location as the M4+ events (Fig. 1). The focal mechanism was determined by the LISUCR using the P-wave polarities and the method proposed by Hardebeck and Shearer (2002). The use of the EGF method allows for the removal of the unknown path and site effects from the observed waveforms, thereby isolating the source time function and rupture characteristics of the main event such as the stress drop, rupture velocity, and rise time.

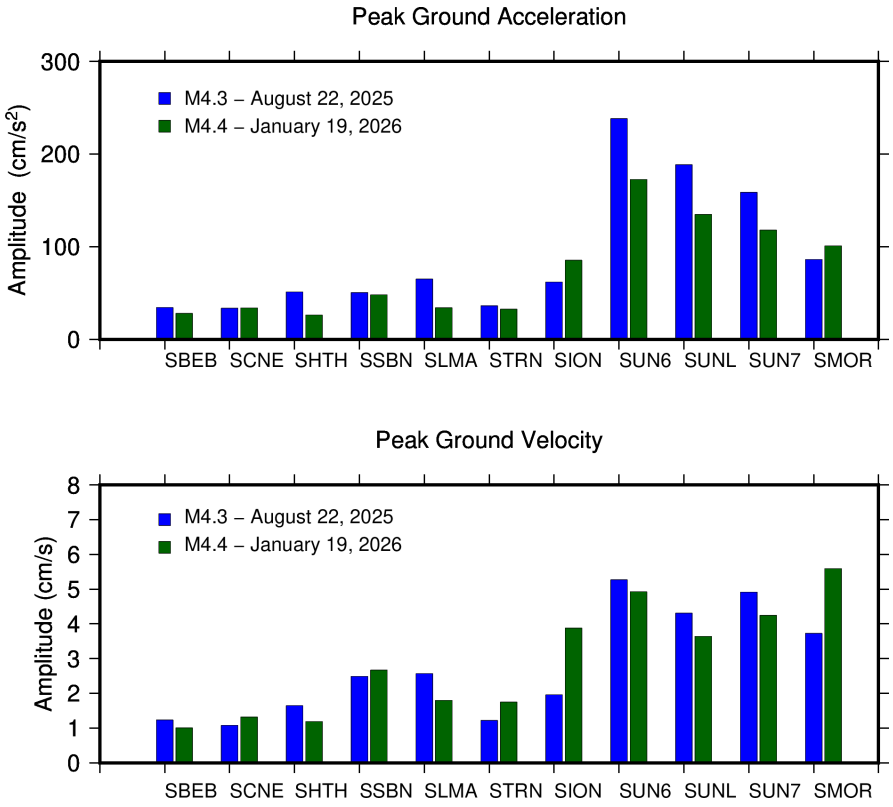

Figure 2. Maximum acceleration and velocity values recorded for the Mw 4.3 and Mw 4.4 events. The stations are ordered from West to East by station code. The values highlight the spatial distribution relative to the hypocenter located between stations STRN and SION.

2. Data and Methods

2.1 Strong Motion Data

The LISUCR maintains a nationwide network of strong-motion instruments that provide continuous records of ground motion from moderate to large earthquakes (Moya et al., 2020). These instruments are located at a variety of sites, and within the GAM there are several dozen stations, including installations in high-rise buildings. Figure 3 shows the distribution of the strong-motion stations throughout the country. The dashed black rectangle shows the study area in Fig. 1.

The network comprises a combination of force-balance accelerometers (FBA) and micro-electromechanical system (MEMS) sensors. FBA sensors are characterized by a wide dynamic range and low self-noise, which allow for reliable integration of acceleration records to velocity and displacement. In contrast, although MEMS sensors provide a cost-effective solution for dense urban deployments and perform adequately for moderate to large ground motions, their higher noise levels limit their ability to accurately capture low-amplitude signals from small events.

For this reason, only stations equipped with FBA sensors were considered in this study. In particular, the SHTH and SLMA stations (highlighted in black in Fig. 1) were excluded from the analysis, as their records exhibit significant noise amplification upon double integration, resulting in unstable and unreliable displacement time series.

2.2 EGF selection

Several aftershocks were evaluated as potential empirical Green's functions (EGFs), as summarized in Table 1. The selection process considered the magnitude, hypocentral proximity to the mainshocks, focal mechanism, and finally, the waveform amplitudes at the selected stations. Table 1 reports the magnitude, depth, and peak ground acceleration (PGA) values at each station. Among the candidates, EGF #8 and #9 were discarded due to missing records at several sites, while EGF #3 (Mw 3.5) was considered too large in source dimension for the events being simulated.

The smallest candidates (EGF #1, #4, and #7) exhibited low PGAs at multiple stations, which compromises their reliability as stable Green's functions, particularly when the waveforms are double-integrated to derive displacement and at more distant stations such as SCNE and SBEB. EGF #2 (Mw 2.8, Depth 3.9 km) was the only candidate with PGA values exceeding 1.5 gals at all stations in addition to being located in the middle of the two mainshocks (Fig. 1).

Table 1. Magnitude, depth (in km) and maximum horizontal PGA values (gals) at given stations for EGF candidates.

Candidate EGF	Mw	Depth	SBEB	SCNE	SION	SMOR	SSBN	STRN	SUNL	SUN6	SUN7
1	2.6	5.0	2.37	0.72	1.41	0.90	0.79	0.70	1.32	2.02	1.80
2	2.8	3.9	3.04	1.51	2.21	1.91	2.55	1.50	5.45	3.03	2.98
3	3.5	3.9	10.47	7.20	12.10	7.81	12.52	6.34	8.77	7.86	8.77
4	2.6	4.4	2.77	0.91	2.38	0.64	1.17	0.75	0.76	0.85	0.45
5	2.8	3.1	1.53	1.18	2.23	1.09	1.60	1.06	0.75	1.11	1.24
6	2.7	5.5	1.60	1.12	0.80	0.91	0.80	0.42	2.50	2.53	1.73
7	2.4	5.2	3.06	0.94	0.71	0.91	1.03	0.38	1.48	1.65	1.17
8	2.9	4.1	4.42	—	5.58	4.37	2.60	—	2.31	2.15	6.54
9	3.5	3.6	6.45	12.31	21.50	—	9.12	—	21.67	—	24.60

We also evaluated the signal-to-noise ratio (SNR) for EGF #2 and the mainshocks. The SNR was calculated as the ratio of the root-mean-square (RMS) amplitude within the signal window to that within a pre-event or post-event noise window. For this analysis, a 10-second window was used. Prior to calculation, all waveforms were detrended, demeaned, and bandpass filtered between 0.1 and 10 Hz. The resulting SNR values for each station are listed in Table 2.

Table 2. Signal to noise ratio (SNR) for selected events at each station.

Event	SBEB	SCNE	SION	SMOR	SSBN	STRN	SUN6	SUN7	SUNL
Mw 2.8	72.5	109.0	44.8	65.8	83.9	51.8	195.9	117.8	115.3
Mw 4.3	63.8	76.7	54.2	77.5	69.4	58.2	110.4	134.9	164.2
Mw 4.4	41.8	46.3	45.5	48.0	42.6	44.5	70.3	66.1	63.2

For the Mw 2.8 event selected as the EGF, the peak ground accelerations (PGA) and peak ground velocities (PGV) show notable variations across stations as shown by Table 3. The eastern stations (SUN6, SUN7, SUNL) exhibit significantly higher PGA and PGV values – 8.14, 2.98, and 5.45 cm/s^2 for PGA, and 0.11, 0.07, and 0.12 cm/s for PGV – compared to western and central stations, where PGA values range from 1.5 to 3.03 cm/s^2 and PGV from 0.02 to 0.05 cm/s. This eastward enhancement is even more pronounced in the mainshocks; for instance, the Mw 4.3 and Mw 4.4 events produced PGAs exceeding 230 cm/s^2 and 170 cm/s^2 respectively at station SUN6. While this shared pattern could be indicative of rupture directivity, the fact that it is present in all three events suggests that local site amplification is an important contributor. The non-uniform scaling between the Mw 2.8 and the larger events, however, indicates that the mainshocks also possess unique source characteristics that could go beyond a simple reflection of the EGF's properties.

Table 3. Horizontal PGA and PGV values for Mw 2.8, Mw 4.3 and Mw 4.4 events.

Station	Mw 2.8		Mw 4.3		Mw 4.4	
	PGA (cm/s^2)	PGV (cm/s)	PGA (cm/s^2)	PGV (cm/s)	PGA (cm/s^2)	PGV (cm/s)
SBEB	3.03	0.02	34.34	1.23	27.98	1.01
SCNE	1.51	0.02	33.49	1.08	33.89	1.32
SION	2.21	0.03	61.89	1.96	85.32	3.88
SMOR	1.91	0.05	86.28	3.72	100.90	5.59
SSBN	2.50	0.04	50.45	2.49	48.00	2.67
STRN	1.50	0.02	36.16	1.22	32.55	1.75
SUN6	8.14	0.11	238.20	5.27	172.60	4.92
SUN7	2.98	0.07	158.60	4.91	117.90	4.25
SUNL	5.45	0.12	188.50	4.31	134.80	3.64

Because of the relatively small amplitude of the velocity waveforms for the study events, the corresponding displacement (PGD), obtained through double integration, would be even smaller and therefore more susceptible to low-frequency noise and baseline errors. To mitigate these effects and ensure stable and reliable time series in the EGF analysis, the frequency band between 0.3 and 10 Hz was used. This frequency range suppresses long-period noise while preserving the signal content relevant for the analysis.

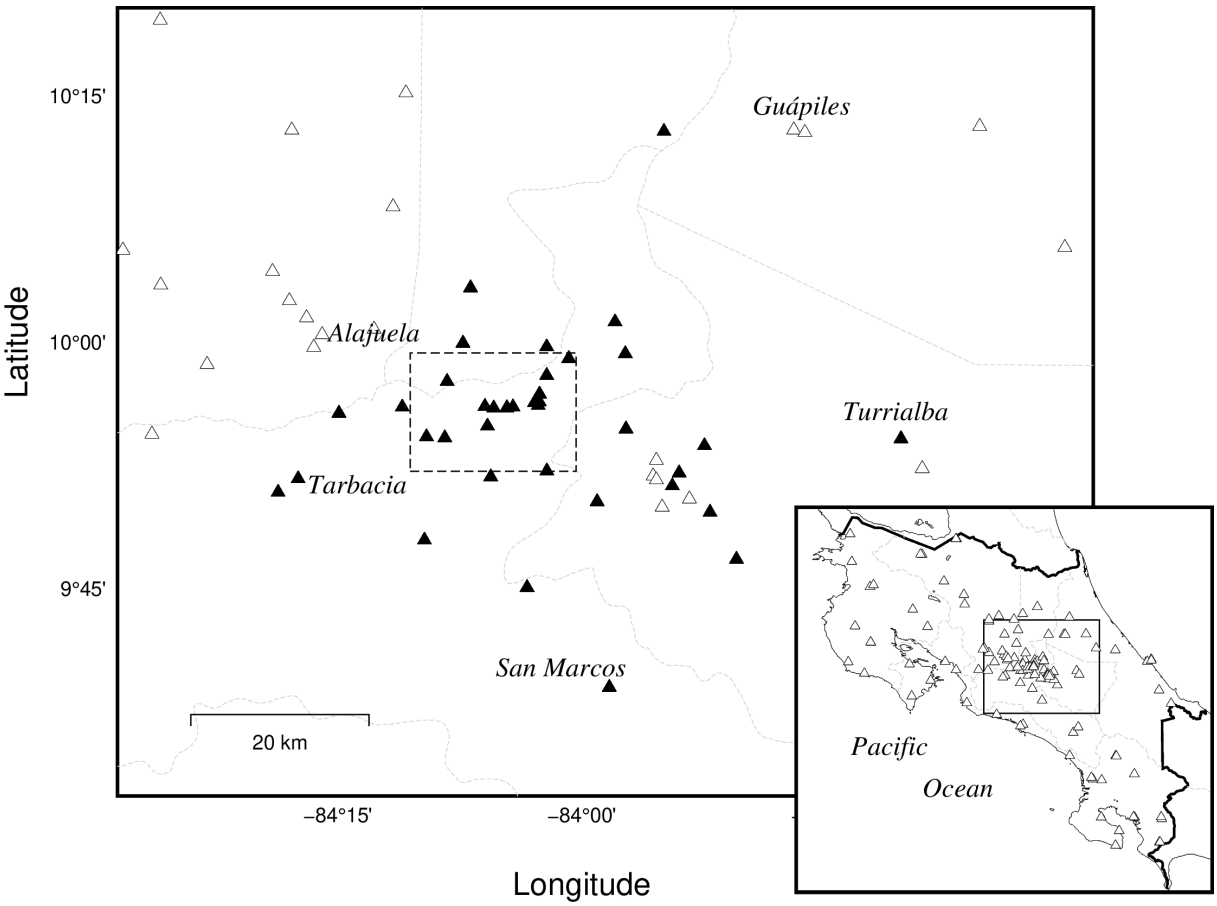

Figure 3. Strong motion station distribution throughout Costa Rica (white triangles). The dashed black box corresponds to the study area shown in Fig. 1. Dashed light gray lines correspond to administrative divisions. Black triangles correspond to stations used to calculate the focal mechanisms.

2.3 Focal mechanism and source parameters

Focal mechanisms were determined using the HASH algorithm (Hardebeck and Shearer, 2002) based on first-motion polarity data. The Mw 2.8 event was constrained by 28 polarity observations, the Mw 4.3 event by 23 polarities, and the Mw 4.4 event by 30 polarities. The station distribution provides generally good azimuthal coverage as shown by the black triangles in Fig. 3 with values of 0.928, 0.876, and 0.978 for the Mw 2.8, Mw 4.3 and, Mw 4.4 events (a value of 1 represents perfect station coverage). The preferred focal mechanism solutions are characterized by low polarity misfit, with values of 6.3%, 4.2%, and 11.3% for the Mw 2.8, Mw 4.3, and Mw 4.4 events, respectively. The corresponding HASH quality grades are B, A, and B which indicate moderate to well-constrained solutions for the purpose of the present study.

Earthquake locations were determined using the non-linear location algorithm NonLinLoc (Lomax et al., 2000). The uncertainties were quantified by the 68% confidence ellipsoids. For the Mw 2.8 event, the semi-major, intermediate, and minor axes of the confidence ellipsoid are 0.97 km, 0.54 km, and 0.55 km, respectively. For the Mw 4.3 event, the corresponding values are 0.77 km, 0.53 km, and 0.42 km, and for the Mw 4.4 event they are 0.80 km, 0.49 km, and 0.53 km. These results indicate that location uncertainties are generally on the order of ~0.4-1.0 km which are small relative to the spatial separation between the events and the stations.

Moment magnitude (Mw) was estimated from low-frequency displacement amplitude spectra following the procedure described in Moya (2024). Spectra were computed for multiple stations, and Mw was obtained from the average spectral level in the low-frequency plateau.

Figure 4 shows the observed displacement, velocity, and acceleration waveforms for the Mw 4.3 (blue trace) and the Mw 4.4 (green trace) events. For both earthquakes, the waveforms exhibit clear, impulsive onsets across

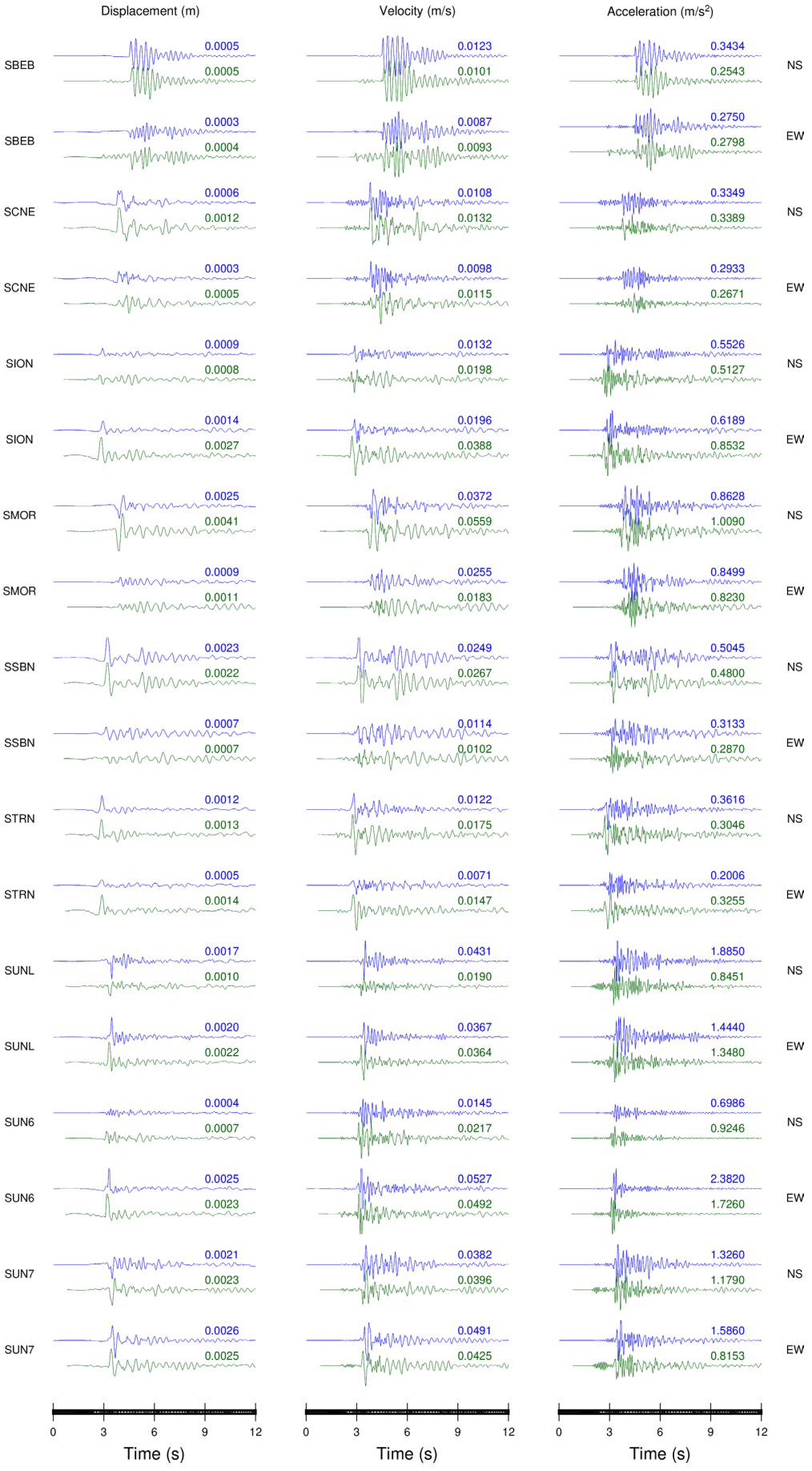

Figure 4. Observed displacement, velocity, and acceleration waveforms for the Mw 4.3 (blue) and Mw 4.4 (green) events.

the network, indicating good signal quality at the selected FBA stations. In the Mw 4.3 event, the observed displacement records are characterized by relatively small peak amplitudes and short signal durations, with most of the energy concentrated within the first few seconds following the initial arrival. The corresponding velocity waveforms show well-defined pulses with peak values generally below a few cm/s, while acceleration records display sharp, high-frequency content with distinct peaks and rapid decays. PGA values range from approximately 30-40 cm/s^2 at western stations such as SBEB and SCNE to more than 200-230 cm/s^2 at eastern stations including SUN6, SUN7, and SUNL.

Waveforms from the Mw 4.4 event display broadly similar characteristics, although displacement records show slightly longer durations and have larger peak amplitudes at several stations (e.g., SUNL, SCNE and SION). Despite the slightly larger magnitude of this event and its closer proximity to several eastern stations, the observed PGA and PGV values are not consistently larger than those of the Mw 4.3 earthquake.

Peak ground motion measurements summarized in Fig. 2 reveal a pronounced azimuthal dependence in shaking intensity for both events. Stations located east of the epicenter record systematically larger PGA and PGV values than stations at comparable distances to the west, whereas western and more distant stations (e.g., SBEB and SCNE) show lower amplitudes and smoother waveform shapes. This spatial pattern is consistent across both mainshocks and is evident in both acceleration and velocity observations.

Normalizing peak ground motions by distance further emphasizes this azimuthal asymmetry (Fig. 5). Eastern stations (azimuths 60-120) exhibit PGA/R and PGV/R values that are 5-10 times larger than those observed at western stations (azimuths 240-300).

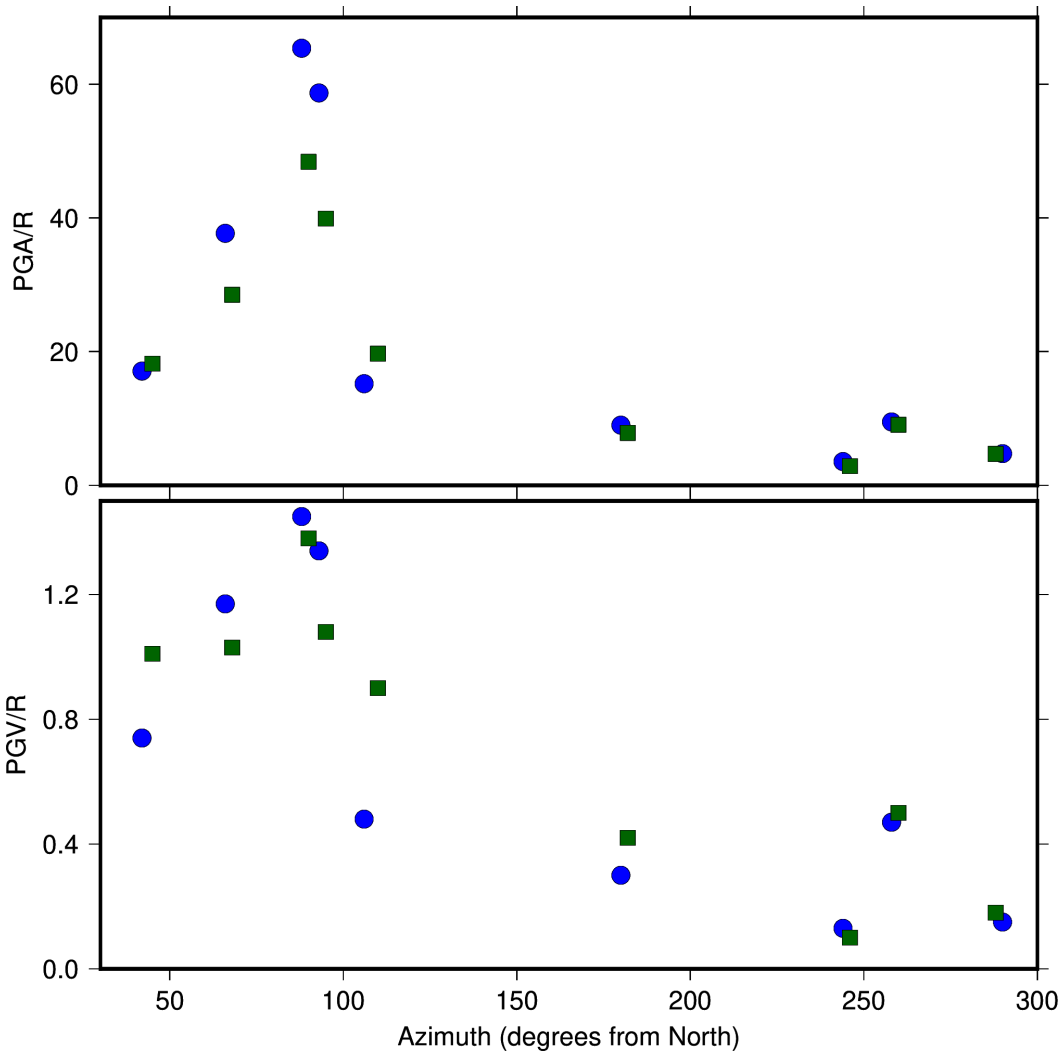

Figure 5. Normalized PGA and PGV values with respect to hypocentral distance, R, as a function of azimuth from north. Mw 4.3 is shown as blue circles, Mw 4.4 is shown as green squares.

The strong similarity of observed waveforms across the network suggests that the two earthquakes likely ruptured the same fault or fault segment, consistent with their similar focal mechanisms and hypocentral locations (Fig. 1 and Table 4). At the same time, systematic differences in amplitude, duration, and relative peak ground motions imply that the rupture processes were not identical, potentially reflecting variations related to them.

Table 4. Location and source parameters for the three events used in the EGF analysis.

	Element event	Mw 4.3	Mw 4.4
Date	2025-08-22 09:21:59	2025-08-22 06:45:37	2026-01-19 23:06:56
Magnitude (Mw)	2.8	4.3	4.4
Depth (km)	3.9	4.0	4.0
Longitude/Latitude	−84.076/9.935	−84.076/9.939	−84.072/9.936
Strike/Dip/Slip	51/56/−20	86/70/−15	76/62/−17

2.4 Empirical Green's Function Method

The empirical Green's function method relies on the assumption that the records from smaller events can be used to reconstruct a larger one as far as they both share similar focal mechanism and hypocentral locations. The rupture process is represented by a finite number of subfaults, N, that corresponds to what Miyake et al. (2003) describe as a strong motion generation area (SMGA). A SMGA is a localized portion of the fault plane that radiates high-frequency seismic energy and controls the generation of near-field strong ground motions. It is characterized by relatively large slip, short rise time, and high stress drop compared to the surrounding rupture area.

Irikura (1986) assumed an omega-squared model (Brune, 1970) to reconstruct the main event ("Mw 4.3" and "Mw 4.4" in Table 4), U(t), as the summation of a smaller event (the "Element event" in Table 4), u(t), distributed along a given number of subfaults, N. In his formulation, the waveform U(t) can be expressed as follows,

$$U(t) = C \sum \sum \frac{r}{r_{ij}} F\left(t - t_{ij}\right) * u(t) \tag{1}$$

$$t_{ij} = \frac{r_{ij} - r_o}{\beta} + \frac{\xi_{ij}}{V_R} \tag{2}$$

$$F(t) = \delta(t) + \frac{1}{n'} \sum \delta \left[t - (k-1) \frac{\tau}{(N-1)n'} \right] \tag{3}$$

where $u(t)$ is the ground-motion from the element event, r, r_{ij}, and r_o are the corresponding distances from the site to the hypocenter, the site to the (i,j) subfault and from the site to the rupture starting point on the fault plane (Fig. 6). ξ_{ij} corresponds to the distance between the starting point and the (i,j) subfault, β is the S-wave velocity, V_r is the rupture velocity, τ is the rise time of the target event, C is the stress drop ratio between the target and element event, and n is an arbitrary integer number used to shift the artificial periodicity to a frequency higher than that of interest. The asterisk in (1) denotes convolution in the time domain.

From the spectral ratio between the observed records from the large and small event, Miyake et al. (2003) proposed the following equation for fitting a theoretical source model such that,

$$SSRF(f) = \frac{M_o}{m_o}\frac{1+\left(\frac{f}{f_a}\right)^2}{1+\left(\frac{f}{f_m}\right)^2} \tag{4}$$

where f_m and f_a correspond to the corner frequency of the large and small magnitude event respectively. If $f \to 0$ then

$$\frac{M_o}{m_o} = CN^3 \tag{5}$$

and when $f \to \infty$

$$\left(\frac{M_o}{m_o}\right)\left(\frac{f_m}{f_a}\right)^2 = CN \tag{6}$$

Then, the N and C constants can be obtained as,

$$N = \frac{f_a}{f_m} \tag{7}$$

$$C = \left(\frac{M_o}{m_o}\right)\left(\frac{f_m}{f_a}\right)^3 \tag{8}$$

For each station, the Fourier amplitude spectrum was calculated. We assumed an S-wave velocity, Vs, of 3.2 km/s and corrected the records by geometrical spreading and quality factor $Q(f) = 179f^{0.5598}$ (Chavarría et al., 2023). We took the vectorial summation $O(f) = \sqrt{(NS(f)^2 + EW(f)^2)}$ of the horizontal components, NS(f) and EW(f). The spectral ratios (Fig. 7) were then computed and a theoretical omega-squared model was fitted to the data using Eq. (4). The corner frequencies estimated from spectral ratios are very similar (8.1 and 7.8 Hz), justifying the use of a common EGF to better isolate source effects (e.g., Wen et al., 2014). Given the small size of the element event, we assumed that the width (w) and length (l) (Fig. 6) were equal, such that w = l = dx. Using the Brune (1970) circular crack model and a corner frequency of ~8 Hz, the source radius was calculated as

$$r = 0.37\frac{Vs}{f_a} \tag{9}$$

The corresponding $dx = \sqrt{(A)} = 0.26$ km, where $A = \pi r^2$. Using Eq. (7) and (8), we obtained N = 3 and C = 5.3 for the Mw 4.3 event and N = 4 and C = 3.2 for the Mw 4.4 event.

A grid-search approach was implemented to determine the optimal rupture initiation point for each SMGA. The search range for the rupture initiation point was 1-3 for the Mw 4.3 event and 1-4 for the Mw 4.4 event. Additionally, rise time was explored within the range 0.01-0.1 s, and rupture velocity, Vr, was varied between 70% and 90% of the shear-wave velocity (Vs). Table 5 summarizes the parameter ranges considered in the analysis.

Table 5. Fixed and searched parameters for EGF analysis.

Parameter	Mw 4.3	Mw 4.4
dx	0.26 km	0.26 km
N	3x3	4x4
C	5.3	3.2
Rise time	0.01-0.1 s	
Vr	0.7Vs-0.9Vs	

We used the following equation proposed by Miyake et al. (2003) to find the residual (res):

$$res = \sum_{1}^{Ns}\sum_{1}^{Nc}\left[\frac{\sum\left(u_{obs}(t)-u_{syn}(t)\right)^2}{\sqrt{\sum u_{obs}(t)^2}\sqrt{\sum u_{syn}(t)^2}}+\frac{\sum\left(a_{obs}(t)-a_{syn}(t)\right)^2}{\sqrt{\sum a_{obs}(t)^2}\sqrt{\sum a_{syn}(t)^2}}\right] \quad (10)$$

where u is the displacement waveform, a is the acceleration envelope, Ns corresponds to the number of stations and Nc to the number of components. In order to give equal weights to the displacement and acceleration waveforms in (10), they were normalized to 1.0. The scenario with the lowest total residual across all stations was identified as the optimal SMGA model.

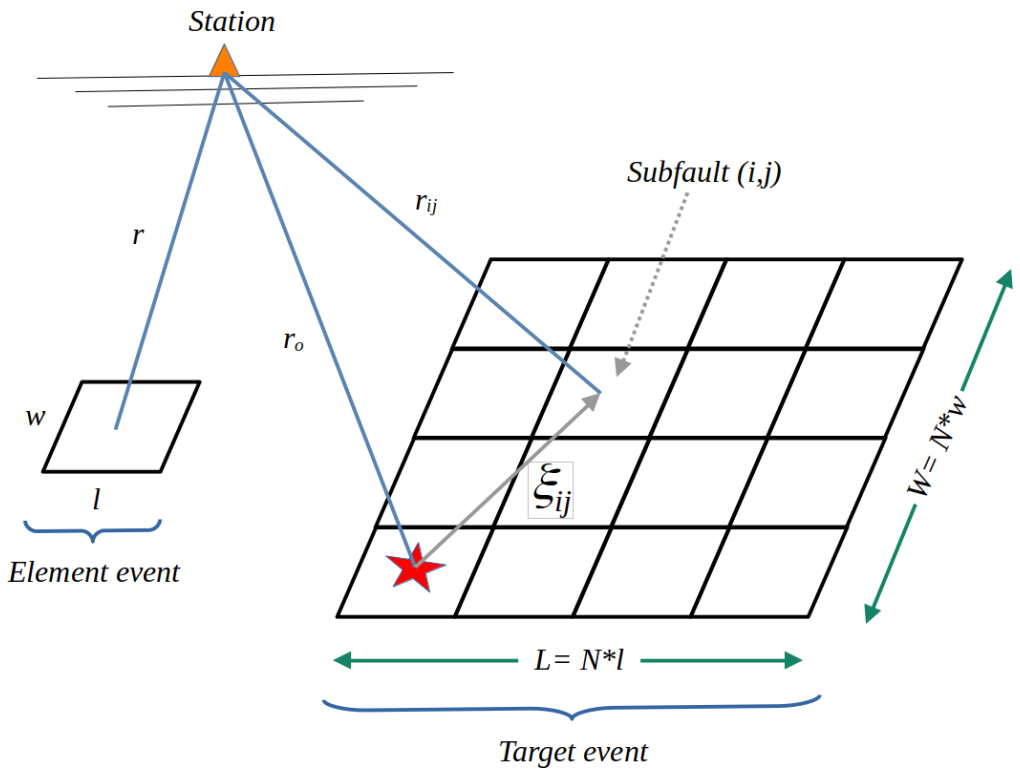

Figure 6. Schematic representation of the empirical Green's function method by Irikura (1986).

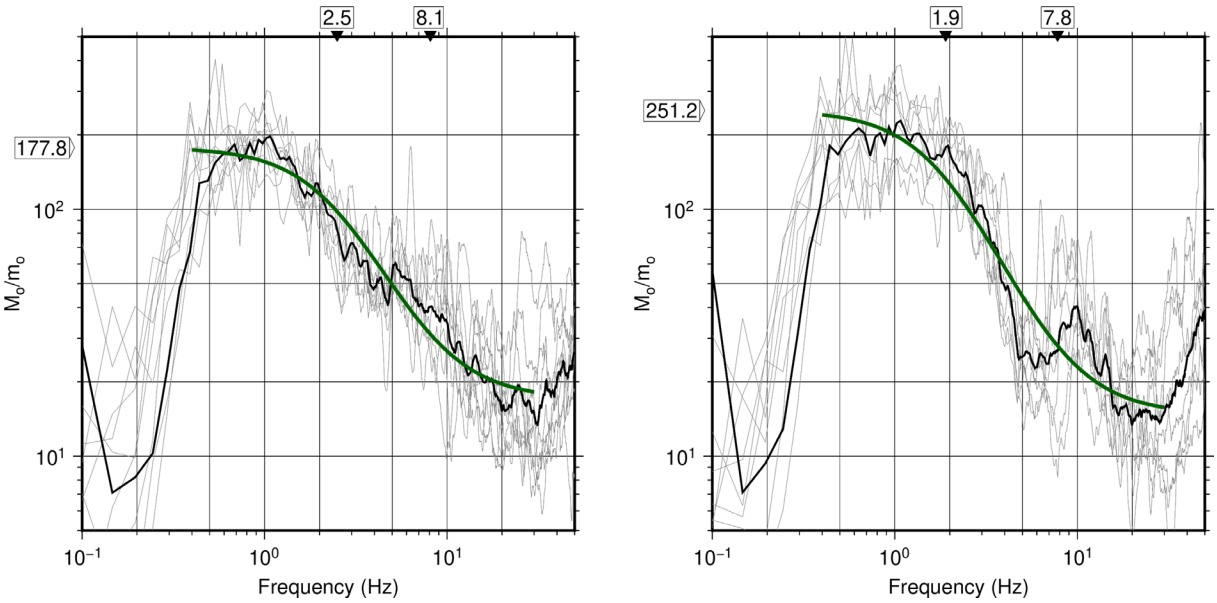

Figure 7. Single spectral ratios between the Mw 4.3/Mw 2.8 (left) and Mw 4.4/Mw 2.8 (right) events at the recording sites (gray lines). The corresponding corner frequencies are shown on top and the ratio between their seismic moments, M_o/m_o, on the left. The thick black line corresponds to the average and the green line to the least-squares fitting following Eq. (4).

3. Results

3.1 Waveform fitting

The observed (black) and synthetic (red) displacement, velocity, and acceleration waveforms for the Mw 4.3 and Mw 4.4 events are shown in Figs. 8 and 9. The quality of the fitting varies among stations and between components. Several stations show agreement in both phase and amplitude, while others show minor discrepancies especially in the later portions of the waveforms, where the synthetics tend to under- or over-estimate secondary arrivals and coda amplitude (in particular at NS component for SUN6 in displacement and SCNE and SBEB). Component-dependent differences are also evident. Figure 10 shows how well the PGA, PGV, and PGD observed values adjust with the synthetic ones. In both events, the EW component seems to be the one with better fits.

Although the Mw 2.8 EGF displays a similar azimuthal pattern to the mainshocks, the focal mechanisms are not identical (Table 4). This suggests that the observed asymmetry in the results for the main events is not a mere reflection of the EGF's characteristics, but also incorporates distinct rupture processes, as evidenced by the different SMGA sizes and stress drops required to fit the synthetic waveforms to the observed ones. Furthermore, the scaling factors between the peak ground motions of the EGF and the mainshocks are not uniform across the network (Table 3). For example, for the Mw 4.3 event, the ground motion at SUN6 increases by a factor of nearly 30, whereas at western stations like SBEB, it only increases by a factor of 10.

The element event's (Mw 2.8) seismic moment was calculated as 2.0E13 N-m; its corresponding stress drop was $\Delta\sigma = 2.77$ MPa. The SMGA's seismic moment was computed as CN^3m_o and the stress drop as $C\Delta\sigma$. Table 6 summarizes the parameters obtained from the grid-search approach for each earthquake. They indicate that the rupture processes were not identical even though the earthquake's magnitude and location were very similar.

For the Mw 4.3 event, the relatively small SMGA area (0.61 km^2), short rise time (0.06 s), and high stress drop (14.7 MPa) could be responsible for the impulsive character and strong high-frequency content of the observed acceleration records. The rupture initiation point at position (1,3), located toward the western portion of the SMGA (Fig. 11), could result in a rupture geometry that enhanced seismic radiation toward the east. This would explain the larger observed PGA and PGV values at eastern stations such as SUN6, SUN7, and SUNL, although peak amplitudes are slightly underestimated at the closest eastern stations, such as SION.

Figure 8. Waveform fitting between observed (black) and synthetic (red) data for both horizontal components in displacement, velocity and acceleration for event Mw 4.3.

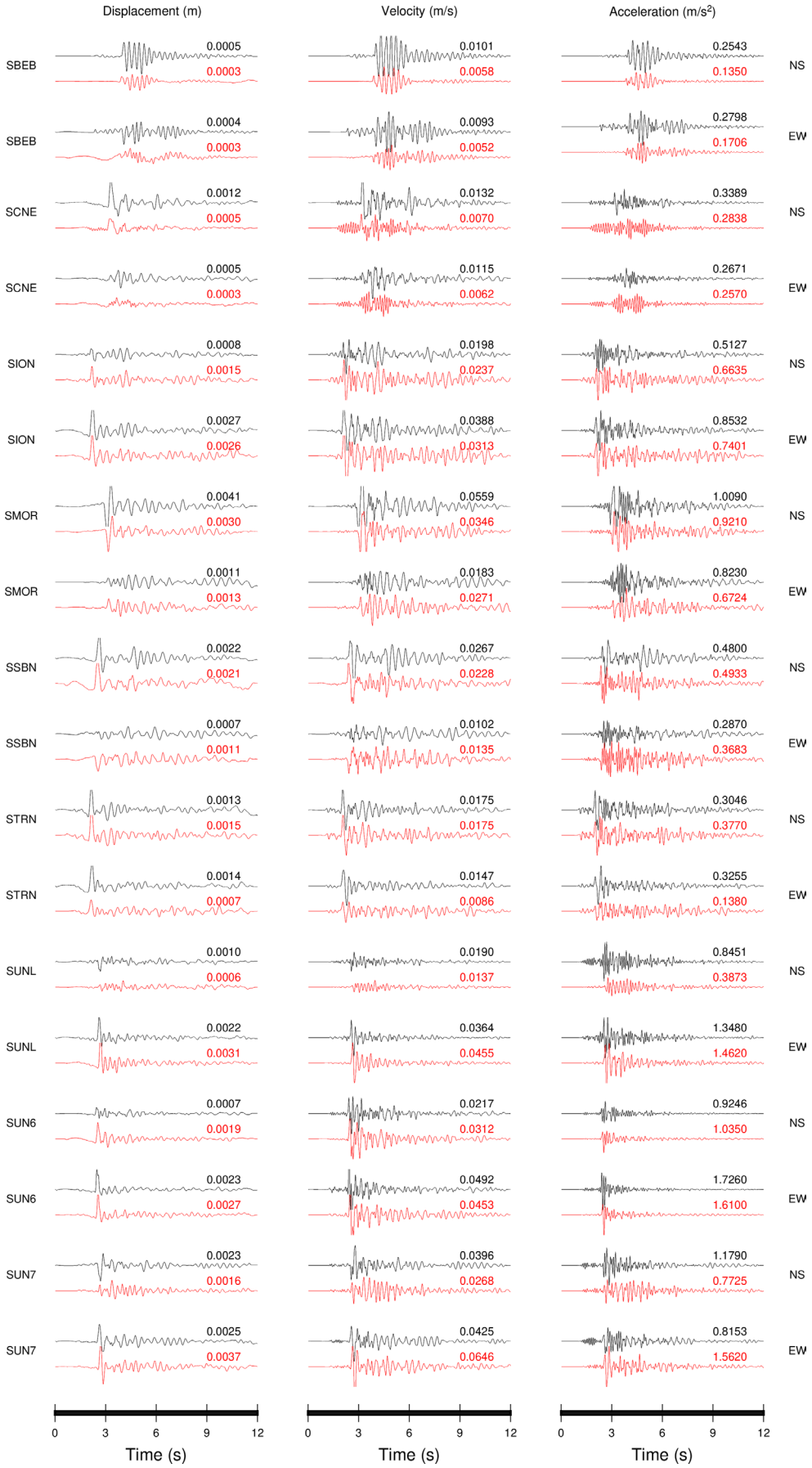

Figure 9. Waveform fitting between observed (black) and synthetic (red) data for both horizontal components in displacement, velocity and acceleration for event Mw 4.4.

On the contrary, the Mw 4.4 event has larger SMGA (1.08 km^2), longer rise time (0.08 s), and lower stress drop (9.98 MPa) that could lead to waveforms with slightly longer durations and smoother envelopes which are observed in displacement and velocity records. The rupture initiation point at (2,4) is deeper and slightly shifted (Fig. 11) compared to that of the Mw 4.3 event. This could result in a different rupture propagation pattern within the SMGA that could produce subtle but systematic differences in waveform amplitude and timing, particularly at intermediate and eastern stations.

Table 6. Source parameters from the EGF determination.

	Mw 4.3	Mw 4.4
SMGA (km^2)	0.61	1.08
Number of subfaults	3x3	4x4
Rupture starting point	(1, 3)	(2, 4)
Rise time (s)	0.06	0.08
Seismic moment of SMGA (N-m)	2.86E15 (Mw 4.3)	4.61E15 (Mw 4.4)
Rupture velocity (km/s)	2.24 (70% of Vs)	2.85 (89% of Vs)
Stress drop (MPa)	14.70	9.98

3.2 Stress drop

Stress drop estimates for small to moderate earthquakes are commonly derived from spectral corner frequencies using circular crack models. Although these estimates exhibit wide variability, typical stress drop values for crustal earthquakes with magnitudes of approximately M3-M4 generally cluster below ~10 MPa. For example, a spectral study of shallow earthquakes in Western Europe by Yen et al. (2024) reported a mean stress drop of ~8.6 MPa for events with $M > 3$, while Bora (2017) found median values of ~5.6-5.8 MPa for shallow crustal earthquakes in the same region. Similarly, Hardebeck and Aron (2009) reported a median stress drop of ~8.7 MPa for M1.0-M4.2 earthquakes along the Hayward Fault in California.

In contrast, the stress drops estimated in this study correspond to the SMGAs. As such, they represent effective stress drops associated with the high-slip, high-radiation portions of the rupture and are expected to be higher than stress drops inferred from whole-source models. Previous studies have shown that SMGA or asperity-based stress drops commonly exceed spectral estimates because they emphasize localized regions of concentrated slip and energy release (e.g., Miyake et al., 2003; Asano and Iwata, 2012). Within this context, the relatively high stress drop of the Mw 4.3 event (~14.7 MPa) is physically reasonable and consistent with the observed impulsive waveforms, whereas the lower stress drop of the Mw 4.4 event (~9.98 MPa), combined with its larger SMGA and longer rise time, probably explain the lower PGA and PGV values compared to the Mw 4.3 event.

Wen et al. (2014) showed that two closely spaced blind-thrust earthquakes in the 2013 Nantou sequence, Taiwan, despite similar magnitudes and focal mechanisms, exhibited distinct strong-motion characteristics associated with different SMGA stress drops (~14 MPa and ~9 MPa). Likewise, Somei et al. (2024) demonstrated for the 2018 Northern Osaka Prefecture earthquake that relatively high SMGA stress drops (~14-15 MPa) and rupture propagation within the SMGA were essential to reproducing observed azimuthal variations in PGA and PGV. This implies that even closely located earthquakes with different stress drops on a similar fault may generate different strong-motion patterns when their SMGA properties differ.

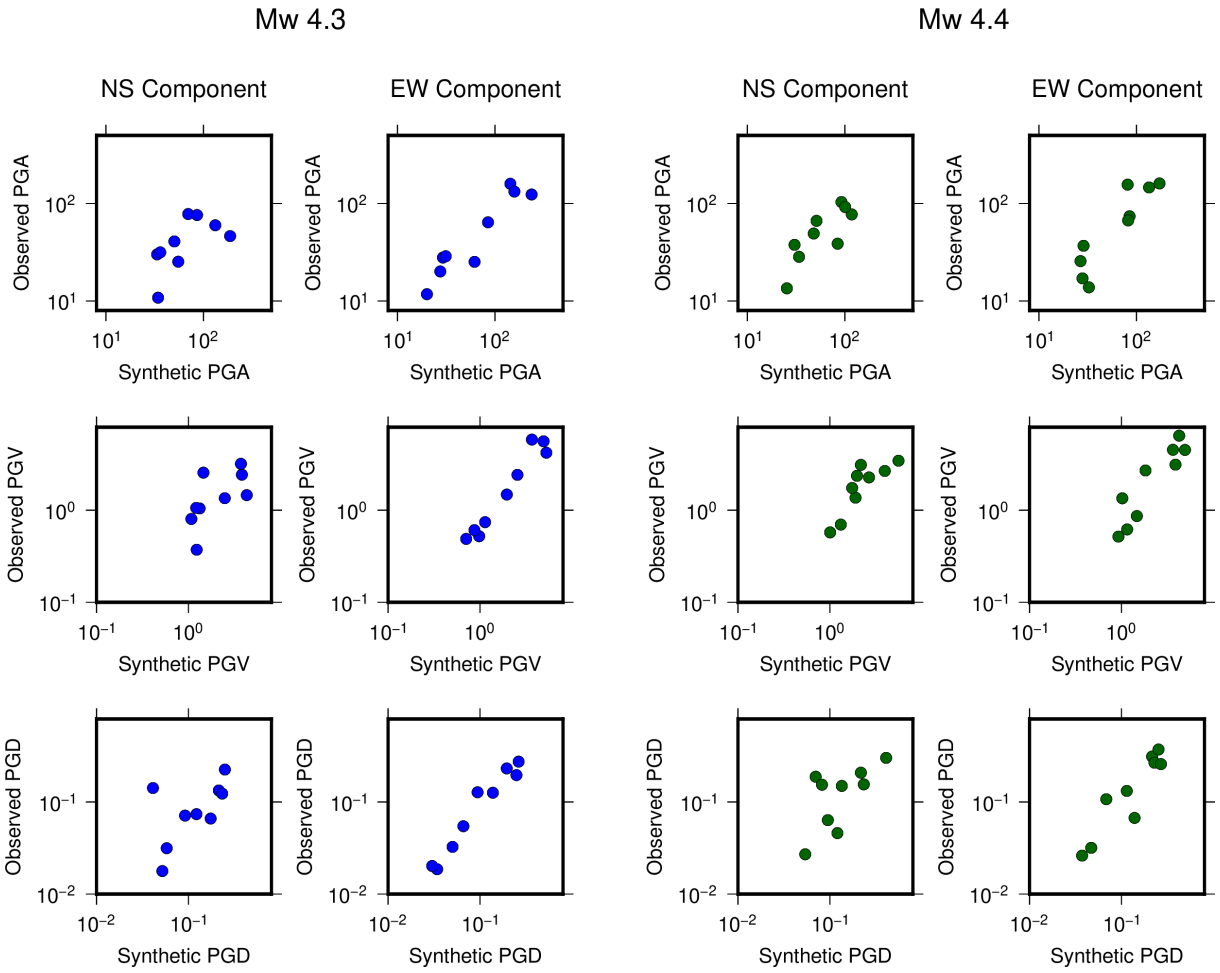

Figure 10. Comparison between observed vs synthetic peak ground displacement, velocity, and acceleration values for the Mw 4.3 (blue circles) and Mw 4.4 (green circles) events.

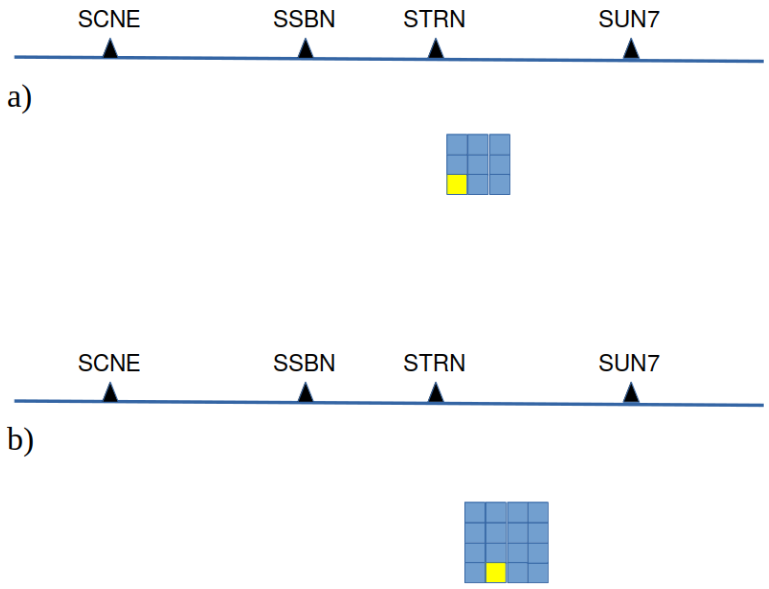

Figure 11. Schematic representation of the SMGAs for the (a) Mw 4.3 and (b) Mw 4.4 earthquakes. The rupture starting point is highlighted in yellow for both events. It is column 1, row 3 (1,3) for the first one and column 2, row 4 (2,4) for the second one. The two earthquakes are located slightly east of STRN station (not to scale, station location is relative).

4. Conclusions

The following conclusions summarize the key findings from this study.

1) The Mw 4.3 and Mw 4.4 earthquakes were likely generated on the same fault or fault segment, as indicated by their similar focal mechanisms, hypocentral locations, and highly coherent observed waveforms from all stations that recorded the events. However, differences in rupture parameters obtained from the simulations confirm that their rupture processes were not identical.

2) Variations in waveform fittings, particularly in later phases and coda, suggest that local site effects, small-scale rupture heterogeneities, and limitations of the simplified source model could contribute to discrepancies between observed and synthetic records. However, the fact that the EGF method successfully simulates the impulsive onsets and the primary wave-shape of the larger events suggests that the SMGA parameters are reasonably well constrained. This means that while the EGF exhibits its own azimuthal amplitude patterns, it still effectively captures the essential path and site responses required to constrain the primary source characteristics of the mainshocks.

3) Source-related parameters – specifically SMGA size, stress drop, rise time, and rupture initiation location – appear to influence the amplitude, frequency content, and duration of the simulated ground motions for both events. The Mw 4.3 event is associated with a smaller SMGA, shorter rise time, and a somewhat higher estimated stress drop, whereas the Mw 4.4 event exhibits a larger SMGA, longer rise time, and a lower estimated stress drop. However, it is important to consider that stress-drop estimates are sensitive to factors such as data quality, modeling assumptions, source parametrization, and possible structural effects. Moreover, the difference between the estimated values (on the order of ~14 MPa versus ~10 MPa) may not be statistically significant, given typical uncertainties that can reach up to a factor of two.

4) An eastward increase in ground-motion amplitudes is observed for all events, with PGA and PGV generally increasing from western to eastern stations. While this pattern offers qualitative support for rupture directivity, the fact that the Mw 2.8 EGF also reflects this tendency suggests that local site conditions may also be a persistent factor. However, the non-uniform scaling of PGA and PGV between the EGF event and the mainshocks (Table 3), combined with the unique SMGA parameters derived for each event, suggests a combined influence of source directivity and site effects. Within the current dataset and analysis framework, the relative contributions of these factors cannot be uniquely separated. Nonetheless, this overall pattern suggests that the eastern sector of the city may represent a zone of elevated seismic hazard.

5) While the station distribution provided a good azimuthal coverage for earthquake location and focal mechanism determination (Fig. 3), no stations north of the study area were used in the EGF analysis (Fig. 1). This limited northern coverage could be a potential source of bias for the radiation pattern interpretation, highlighting the need for future northern expansions of the LISUCR network to fully constrain the rupture geometry of potential events in central San José.

6) Western stations show relatively uniform distance-normalized PGA and PGV values between the two events, suggesting more stable ground-motion levels in that azimuth. In contrast, eastern stations display greater variability, which may reflect a combination of source radiation effects, local site conditions, and the spatial distribution of stations used in the analysis.

7) The lower-magnitude (Mw 4.3) earthquake produced higher peak ground accelerations than the slightly larger (Mw 4.4) event at several stations, particularly toward the east. This peculiarity cannot be explained solely by stress-drop differences. It is likely influenced by rupture directivity, SMGA geometry, and azimuthal variations in ground-motion radiation, combined with local site effects. This observation highlights that magnitude alone does not determine peak amplitudes and emphasizes the importance of detailed source modeling for realistic ground-motion simulations.

8) The optimization algorithm used in this study was designed to minimize residuals in waveform fitting using Eq. (10). However, we recognize that a potential trade-off between seismic moment and corner frequency during the initial spectral fitting stage could influence the calculated stress-drop values (Fig. 7). Because stress drop is highly sensitive to corner frequency (Eq. 9), the estimates obtained in this study should be interpreted with caution.

Data availability statement. Strong motion data is available at https://crsmd.lis.ucr.ac.cr/. A program of the empirical Green's function method by Irikura (1986) can be provided upon request to the author.

Acknowledgments. We thank the two anonymous reviewers for their rigorous review and valuable suggestions, which helped improve the robustness of this manuscript. We are grateful for the dedicated work of the technicians responsible for maintaining the strong-motion network over the years: Carlos Segura, Esteban Cordero, Arturo Jiménez, Andrés Fallas, Gabriel Solano, Luis Navarro, and Gustavo Poveda.

References

Alonso-Henar, J., W. Montero, J. J. Martínez-Díaz and J. A. Alvarez-Gómez (2013). The Aguacaliente fault, source of the Cartago 1910 destructive earthquake (Costa Rica), Terra Nova, 25, 5, 368-373, doi:10.1111/ter.12045.

Asano, K. and T. Iwata (2012). Source model for strong ground motion generation in the frequency range 0.1-10 Hz during the 2011 Tohoku earthquake, Earth Planets Space, 64, 1111-1123, doi:10.5047/eps.2012.05.003.

Barquero, R. (2009). El terremoto de Cinchona del jueves 8 de enero de 2009, Rev. Geol. Am. Cent., 40, 91-95, doi:10.15517/rgac.v0i40.4188.

Benito, M. B., M. Arroyo-Solórzano, A. Clíment, W. Montero et al. (2025). Seismic hazard scenarios for the city of San José, Costa Rica: Evaluation of critical ruptures on nearby faults, Earthq. Spectra, 41, 3, 2335-2370, doi:10.1177/87552930251319736.

Bora, S. S., F. Cotton, F. Scherbaum, B. Edwards et al. (2017). Stochastic source, path and site attenuation parameters and associated variabilities for shallow crustal European earthquakes, Bull. Earthq. Eng., 15, 4531-4561, doi:10.1007/s10518-017-0167-x.

Brune, J. N. (1970). Tectonic stress and the spectra of seismic shear waves from earthquakes, J. Geophys. Res., 75, 26, 4997-5009, doi:10.1029/JB075i026p04997.

Chavarría, N., T. Yokoi and T. Hayashida (2023). Strong motion estimation in Costa Rica at non-record sites using spectral inversion method, J. Seismol., 27, 305-324, doi:10.1007/s10950-023-10137-9.

Clíment, A., W. Rojas, G. E. Alvarado and B. Benito (2008). Proyecto Resis II: Evaluación de la amenaza sísmica en Costa Rica, UPM, NORSAR, San José, Costa Rica, https://rsn.ucr.ac.cr/images/Biblioteca/Informes_sismos/amenaza_Sísmica_cr.pdf. Accessed 05 Feb 2026.

Fernández, M. and W. Montero (2002). Fallamiento y sismicidad del área entre Cartago y San José, Valle Central de Costa Rica, Rev. Geol. Am. Cent., 26, 25-37, doi:10.15517/rgac.v0i26.8528.

Hardebeck, J. L. and A. Aron (2009). Earthquake stress drops and inferred fault strength on the Hayward Fault, East San Francisco Bay, California, Bull. Seismol. Soc. Am., 99, 1801-1814, doi:10.1785/0120080242.

Hardebeck, J. L. and P. M. Shearer (2002). A new method for determining first-motion focal mechanisms, Bull. Seismol. Soc. Am., 92, 6, 2264-2276, doi:10.1785/0120010200.

Hidalgo-Leiva, D., L. Linkimer, I. Arroyo, M. Arroyo-Solórzano et al. (2022). The 2022 seismic hazard model for Costa Rica, Bull. Seismol. Soc. Am., 113, 1, 23-40, doi:10.1785/0120220119.

Irikura, K. (1986). Prediction of strong acceleration motion using empirical Green's function, in Proc. 7th Japan Earthquake Engineering Symposium, Tokyo, 151-156.

Lomax, A., J. Virieux, P. Volant and C. Berge-Thierry (2000). Probabilistic Earthquake Location in 3D and Layered Models, in Advances in Seismic Event Location, Modern Approaches in Geophysics C. H. Thurber and N. Rabinowitz (Eds.), 18, Springer, Dordrecht, doi:10.1007/978-94-015-9536-0_5.

Miyake, H., T. Iwata and K. Irikura (2003). Source characterization for broadband ground-motion simulation: Kinematic heterogeneous source model and strong motion generation area, Bull. Seismol. Soc. Am., 93, 2531-2545, doi:10.1785/0120020183.

Montero, W. and S. Miyamura (1981). Distribución de intensidades y estimación de los parámetros focales de los terremotos de Cartago de 1910, Costa Rica, América Central, Inf. Sem. IGN, 2, 9-34.

Moya, A., L. A. Pinzón, V. Schmidt-Díaz, D. Hidalgo-Leiva et al. (2020). A strong-motion database of Costa Rica: 20 years of digital records, Seismol. Res. Lett., 91, 3407-3416, doi:10.1785/0220200036.

Moya, A. (2024). The MASLIS: A five-year review of Costa Rica's near real-time seismic intensity processing system, Ann. Geophys., 67, 5, S552, doi:10.4401/ag-9137.

OVSICORI-UNA (2026). Reporte de actividad sísmica: Estudio preliminar de la actividad sísmica en el centro de San José entre agosto de 2025 y enero de 2026, Accessed 05 Feb 2026, https://www.ovsicori.una.ac.cr/index.php/sismologia/informes-y-boletines/boletines sismologia?download=1295:reporte-de-actividad-Sísmica-estudio-preliminar-de-la-actividad-Sísmica-en-el-centro-de-san-José-entre-agosto-de-2025-y-enero-de-2026.

Peraldo, G. and W. Montero (1999). Sismología histórica de América Central, Instituto Panamericano de Geografía e Historia-UCR, 348, ISBN:9789686384321.

Quesada Román, A. and G. Barrantes Castillo (2016). Procesos de ladera cosísmicos del terremoto de Cinchona (Costa Rica) del 8 de enero de 2009 (Ms = 6.2), Cuad. Geogr., 25, 1, 217-232.

Red Sismológica Nacional, RSN (2026). Sismos en San José, enero de 2026, https://rsn.ucr.ac.cr/index.php/actividad-Sísmica/reportes-sismicos/sismo-en-san-José-19-de-enero-de-2026, Accessed 05 Feb 2026.

Somei, K., Y. Guo, K. Yoshida, T. Akazawa et al. (2024). Reproductions of strong ground motions during the 2018 Northern Osaka Prefecture earthquake using the empirical Green's function method, Japan Geotech. Soc. Spec. Publ., 10, 60, 2465-2468, doi:10.3208/jgssp.v10.P2-22.

Yen, M. H., D. Bindi, A. Oth, B. Edwards et al. (2024). Source parameters and scaling relationships of stress drop for shallow crustal seismic events in Western Europe, J. Seismol., 28, 63-79, doi:10.1007/s10950-023-10188-y.

Wen, Y. Y., H. Miyake, Y. T. Yen, K. Irikura et al. (2014). Rupture directivity effect and stress heterogeneity of the 2013 Nantou blind-thrust earthquakes, Taiwan, Bull. Seismol. Soc. Am., 104, 6, 2933-2942, doi:10.1785/0120140109.

***CORRESPONDING AUTHOR: Aaron MOYA**,
Universidad de Costa Rica, Laboratorio de Ingeniería Sísmica, Costa Rica
e-mail: cesar.moya@ucr.ac.cr
© 2026 the Author(s). All rights reserved.
Open Access. This article is licensed under a Creative Commons Attribution 4.0 International